JACS
JOURNAL OF THE AMERICAN CHEMICAL SOCIETY
Article
pubs.acs.org/JACS

Boosting the Thermoelectric Performance of (Na,K)-Codoped Polycrystalline SnSe by Synergistic Tailoring of the Band Structure and Atomic-Scale Defect Phonon Scattering

Zhen-Hua Ge,[†,‡] Dongsheng Song,[‡,§] Xiaoyu Chong,[†,‡,∥] Fengshan Zheng,[*,⊥] Lei Jin,[⊥] Xin Qian,[#] Lei Zheng,[#] Rafal E. Dunin-Borkowski,[⊥] Peng Qin,[†] Jing Feng,[*,†] and Li-Dong Zhao[*,#]

[†]Faculty of Materials Science and Engineering, Kunming University of Science and Technology, Kunming 650093, China
[§]National Center for Electron Microscopy in Beijing, School of Materials Science and Engineering, Tsinghua University, Beijing 100084, China
[⊥]Ernst Ruska-Centre for Microscopy and Spectroscopy with Electrons and Peter Grünberg Institute, Forschungszentrum Jülich, 52425 Jülich, Germany
[#]School of Materials Science and Engineering, Beihang University, Beijing 100191, China
[∥]Department of Materials Science and Engineering, The Pennsylvania State University, University Park, Pennsylvania 16802, United States

Supporting Information

ABSTRACT: We report the high thermoelectric performance of p-type polycrystalline SnSe obtained by the synergistic tailoring of band structures and atomic-scale defect phonon scattering through (Na,K)-codoping. The energy offsets of multiple valence bands in SnSe are decreased after Na doping and further reduced by (Na,K)-codoping, resulting in an enhancement in the Seebeck coefficient and an increase in the power factor to 492 μW m^{-1} K^{-2}. The lattice thermal conductivity of polycrystalline SnSe is decreased by the introduction of effective phonon scattering centers, such as point defects and antiphase boundaries. The lattice thermal conductivity of the material is reduced to values as low as 0.29 W m^{-1} K^{-1} at 773 K, whereas ZT is increased from 0.3 for 1% Na-doped SnSe to 1.2 for 1% (Na,K)-codoped SnSe.

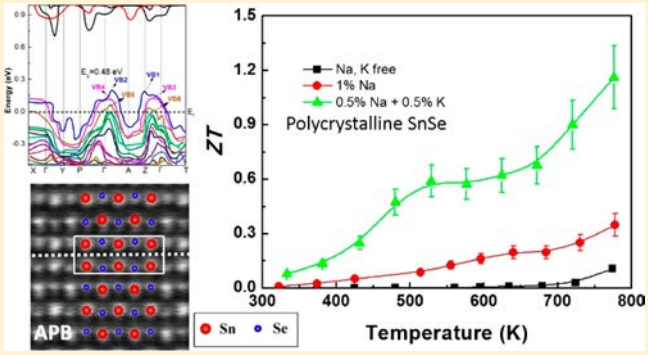

1. INTRODUCTION

Thermoelectric materials can convert heat into electricity directly and have the potential to impact power generation significantly. Thermoelectric conversion efficiency is described by the dimensionless figure of merit $ZT = \frac{\sigma S^2}{\kappa}T$, where S is the Seebeck coefficient, σ is the electrical conductivity, κ is the total thermal conductivity including contributions from phonons (κ_{lat}) and carriers (κ_{ele}), and T is the absolute temperature.[1] Great effort has been devoted to boosting the thermoelectric conversion efficiencies of materials, both by enhancing the power factor (σS^2) and by decreasing the thermal conductivity. The power factor can be optimized by band engineering,[2,3] whereas the lattice thermal conductivity can be suppressed by the use of hierarchical architectures[4] through all-length-scale phonon scattering.[5]

The Earth-abundant low-toxicity binary compound SnSe has attracted significant attention in the thermoelectric community as a result of its high value of ZT (~2.6 at 923 K) along the crystallographic b axis.[6] Its low thermal conductivity has been attributed to anharmonic bonding, that is, to a high Grüneisen parameter, in the layered crystal structure.[6−9] A high value of ZT (~2.0 at 773 K and ~1.34 in a device over the temperature range of 300 to 773 K) was achieved in Na-doped crystalline SnSe and attributed to an increased power factor resulting from the activation of multiple valence bands.[10,11] However, polycrystalline SnSe is, in principle, a better choice for such applications, in part because of its ease of production and machinability. Therefore, considerable effort has been focused on improving the thermoelectric performance of polycrystalline SnSe.[12−21] Alkali elements,[12−16] Ag,[13,17] I,[18] Br,[19] and $BiCl_3$[20] have all proven to be effective dopants in both p-type and n-type polycrystalline SnSe. Doping with Na has proved to be particularly effective in increasing the thermoelectric performance of p-type polycrystalline SnSe.[16,17] A maximum value for ZT of ~0.8 was realized below 800 K in ~1% Na-doped polycrystalline SnSe[13,16] and associated with a lowering of the

Received: May 24, 2017
Published: June 21, 2017

DOI: 10.1021/jacs.7b05339
J. Am. Chem. Soc. 2017, 139, 9714−9720

Fermi level to activate multiple valence bands while at the same time introducing point defects and nanoscale precipitates to increase phonon scattering.[10,13,16] K doping has also been proved to be effective at increasing the carrier concentration,[16] resulting in a maximum value for ZT of ∼1.1 at 773 K,[15] both by preventing the formation of tin oxide and by precipitating nanostructures to scatter phonons. However, the function of K is not yet fully understood. These results motivated us to investigate SnSe polycrystals, with Na selected as a dopant to enhance the electrical transport and K selected as a codopant with Na to reduce the thermal conductivity.

Surprisingly, we found that (Na,K)-codoping not only introduces defects into the SnSe matrix but also increases the solid solubility of Na and K when compared to the use of Na doping alone. Specifically, the solid solubility of 0.5% Na + 0.5% K in SnSe is higher than that of 1% Na. The Seebeck coefficient is enhanced as a result of the activation of multiple valence bands, whereas the thermal conductivity is reduced as a result of scattering from atomic-scale structural defects. High thermoelectric performance is achieved in polycrystalline SnSe by simultaneously enhancing the power factor and suppressing the thermal conductivity. A value of ZT of ∼1.2 was measured at 773 K, which is the highest value reported in polycrystalline SnSe.

2. RESULTS AND DISCUSSION

2.1. Structural Characterization. The low-temperature phase of SnSe adopts a layered orthorhombic crystal structure with space group *Pnma* (No. 62) and lattice constants a = 11.49 Å, b = 4.44 Å, and c = 4.135 Å. X-ray diffraction (XRD) patterns recorded from the three samples prepared in this work were indexed to the SnSe *Pnma* phase (Figure S1a). Peaks from the doped samples were shifted slightly to the right when compared to those from the undoped samples, indicating that the lattice constants had decreased. As shown in Figure S1c, the lattice constants of the bulk sample decreased when it was doped with Na, in agreement with the shift in the diffraction peak position. The lattice constants decreased further upon doping with both Na and K, suggesting that the total solid solubility of 0.5% Na + 0.5% K is higher than that of 1% Na. The changes in lattice constant can be related to the ionic radii of Na (102 pm), K (138 pm), and Sn (112 pm).

Aberration-corrected scanning transmission electron microscopy (STEM) was used to visualize the Sn/Se slabs stack along the a axis. Figure 1 shows representative high-resolution STEM high-angle annular dark-field (HAADF) images viewed along the b [010] and c [001] zone axes. Image simulations[30] are shown in the insets. The two-atom-thick slabs, which are indicated by dashed rectangles in Figure 1, are corrugated along the c axis, resulting in a zigzag-like projection in Figure 1a. In contrast, the atomic configuration along the b axis is much less indented, as shown in Figure 1b, suggesting that this might be the highest-mobility direction.[10] Atomic-scale STEM HAADF and energy-dispersive X-ray spectroscopy (EDS) mapping along the b [010] zone axis was further performed to confirm the chemical information in an FEI Titan ChemiSTEM 80−200 transmission electron microscope equipped with a Super-EDX detector and an ultrabright field-emission gun,[31] as shown in Figure 1c−f.

2.2. Solid Solubility and Band Structure. *2.2.1. Solid Solubility.* It is believed that many conventional dopants cannot be used to effectively dope Sn sites in SnSe as a result of its anisotropic layered structure and, hence, limited solid

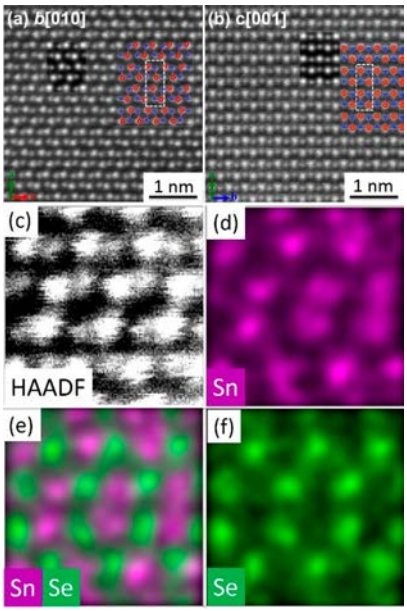

Figure 1. (a,b) High-resolution STEM HAADF images of SnSe viewed along (a) b [010] and (b) c [001]. The overlays show Sn atoms in red and Se atoms in blue. A single unit cell is indicated by the dashed rectangle. The insets show simulated STEM HAADF images. (c−f) Atomic-scale energy-dispersive X-ray spectroscopy (EDS) mapping from the zone axis [010] in the SnSe sample.

solubility.[13,26] Ag,[11,17] Li,[16] Na,[10−14,16] and K[15,16] have been reported to be effective dopants, although with limited solid solubility. Na is widely used, in part because it effectively increases the power factor by pushing down the Fermi level and enabling multiple valence-band contributions to the optimization of the electrical conductivity and the Seebeck coefficient.[10,11] TEM observations in the present work showed that there were more precipitates in the doped samples than in undoped SnSe. Hence, the solid solubility of Na in SnSe is expected to be lower than 1%, with only some of it being incorporated into the SnSe lattice and the rest remaining as precipitates,[15,16] although this conclusion might be specific to chemical synthesis.[24] Figure 2 shows low-magnification TEM images of the doped samples, viewed along the [001] zone axis and indexed according to the inset electron diffraction patterns. In the (0.5% Na+0.5% K)-codoped sample, the precipitates are smaller and their number density is lower than in the 1% Na-

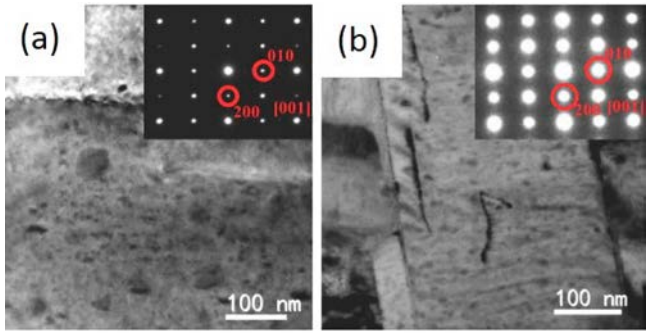

Figure 2. Low-magnification bright-field TEM images of precipitate distributions in the (a) 1% Na-doped and (b) (0.5% Na+0.5% K)-codoped SnSe samples. The insets show corresponding indexed electron diffraction patterns.

DOI: 10.1021/jacs.7b05339
J. Am. Chem. Soc. 2017, 139, 9714−9720

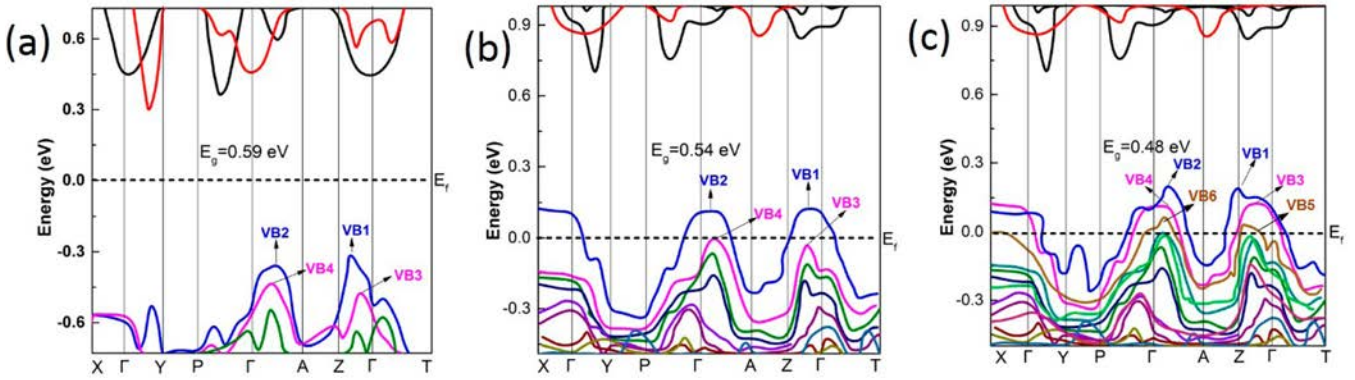

Figure 3. DFT-calculated band structures in (a) undoped, (b) 1% Na-doped, and (c) (0.5% Na+0.5% K)-codoped SnSe.

doped sample. This observation suggests that the solid solubility of 0.5% Na + 0.5% K is higher than that of 1% Na, in agreement with the XRD lattice parameters.

To understand the difference between the Na and K solubility limits in SnSe, as well as the effects of Na and K codoping, we used density functional theory (DFT) to calculate the solubility limits of Na and K in SnSe (see details in the Supporting Information). The defect formation energies, ΔE_F^{def}, for Na and K solute atoms in SnSe can be determined from the expression[25]

$$\Delta E_F^{def} = (E_{SnSe}^{def} - E_{SnSe}^{pure} - \mu_A^0 + \mu_{Sn}^0) - (\Delta\mu_A - \Delta\mu_{Sn}) \quad (1)$$

where A = Na or K; ΔE_{SnSe}^{def} is the DFT-calculated total energy of a SnSe supercell containing one Na or K atom; ΔE_{SnSe}^{pure} is the DFT-calculated total energy of a pure SnSe supercell; the quantities μ_A^0 and μ_{Sn}^0 are the chemical potentials of A and Sn, respectively, in their standard metallic states; and the quantities $\Delta\mu_A$ and $\Delta\mu_{Sn}$ are the changes in the chemical potentials of A and Sn, respectively, resulting from the equilibrium between SnSe and ASe, obtained from the corresponding compounds in thermodynamic equilibrium for the composition of the defect system. The substitution of Na or K for Sn in SnSe places the system on the pseudobinary tie line between SnSe and ASe. The equilibrium between the compounds can be used to determine the changes in μ_A and μ_{Sn} relative to the elements.

Table S2 shows the defect formation energies of 1 Na atom or 1 K atom in a 200-atom supercell and of 1 Na atom with 1 K atom in a 400-atom supercell of SnSe. ΔE_F^{def} is negative for 1% Na-doped SnSe but positive for 1% K-doped SnSe and (Na, K)-codoped SnSe. Codoping decreases ΔE_F^{def} to half of the value for 1% Na-doped SnSe, suggesting that the substitution of Na for Sn in SnSe might increase the dilute-limit solubility of Na in (Na, K)-codoped SnSe. The negative value for Na suggests that the formation of a Sn−Na−Se ternary compound might change the equilibrium state and raise ΔE_F^{def} for Na on the Sn site in SnSe, which might explain why there are precipitates in 1% Na-doped SnSe. Moreover, the solid solubility is expected to be related to the synthesis method. It has been reported that the solubility of Na in polycrystalline SnSe is lower than that in single crystals of SnSe.[10,16,24] The dilute-limit solubility of K in SnSe can be estimated to be approximately 0.7 mol % at 500 K from the expression $\exp(-\Delta E_F^{def/k_BT})$, where k_B is the Boltzmann constant. The fact that the solubility at 500 K is lower than 1 mol % suggests that more K will form as precipitates than substitute for Sn in the matrix, in agreement with a previous report.[15] The defect formation energy in (0.5% Na+0.5% K)-codoped SnSe is only one-quarter of the value in the K-doped sample, suggesting that Na will help K to substitute more Sn in the matrix, in agreement with the XRD lattice parameter analysis.

2.2.2. Band Structure. Doping with different alkali elements changes the electronic structure of SnSe, as indicated by first-principles DFT electronic structure calculations.[22] In the Na-doped sample, the Fermi level is shifted down into the two main valence bands, VB1 and VB2, and approaches VB3 and VB4, as shown in Figure 3b. Surprisingly, Figure 3c shows that the Fermi level in the (0.5% Na+0.5% K)-codoped sample is shifted much lower into the valence bands (into six bands) than in the Na-doped sample. The carrier pockets near the Fermi level (when multiple bands have energies equal or comparable to $\sim k_BT$, 0.026 eV at 300 K) contribute to the Seebeck coefficient,[25] as was also found in (Na,Ag)-doped SnSe,[10,11] not only for the two top valence bands VB1 and VB2 but also for lower-lying valence bands. Table 1 lists the energy differences between the approaching valence bands, which are on the order of k_BT, suggesting that the low-lying bands VB3 and VB4 in the Na-doped sample and VB3−VB6 in the (0.5% Na+0.5% K)-codoped sample can contribute to electrical transport. It should be noted that the energy differences are suppressed due to doping. For example, VB4 − VB3 decreases from 0.030 eV in the undoped sample to 0.029 and 0.023 eV in the Na-doped and (0.5% Na+0.5% K)-codoped samples, respectively.

Table 1. Calculated Energy Differences between Valence Bands in Undoped, 1% Na-Doped, and (Na, K)-Codoped SnSe

	ΔE (eV)		
sample	VB2 − VB1	VB4 − VB3	VB6 − VB5
undoped	0.021	0.030	–
1% Na	0.015	0.029	–
0.5% Na + 0.5% K	0.014	0.023	0.041

2.3. Enhancement of the Power Factor through Band Engineering. Figure 4 shows the electrical transport properties of undoped and doped polycrystalline SnSe, which were measured perpendicular to the pressing direction used during spark plasma sintering (SPS). The electrical conductivity increased dramatically in each of the doped samples, from 0.002 S/cm in the undoped sample to 10.646 and 14.100 S/cm at 323 K as the carrier concentration was increased from almost 2.2×10^{16} cm^{-3} to 4.8×10^{19} and 7.2×10^{19} cm^{-3} in the Na-doped and (Na,K)-codoped SnSe samples, respectively, as

DOI: 10.1021/jacs.7b05339
J. Am. Chem. Soc. 2017, 139, 9714−9720

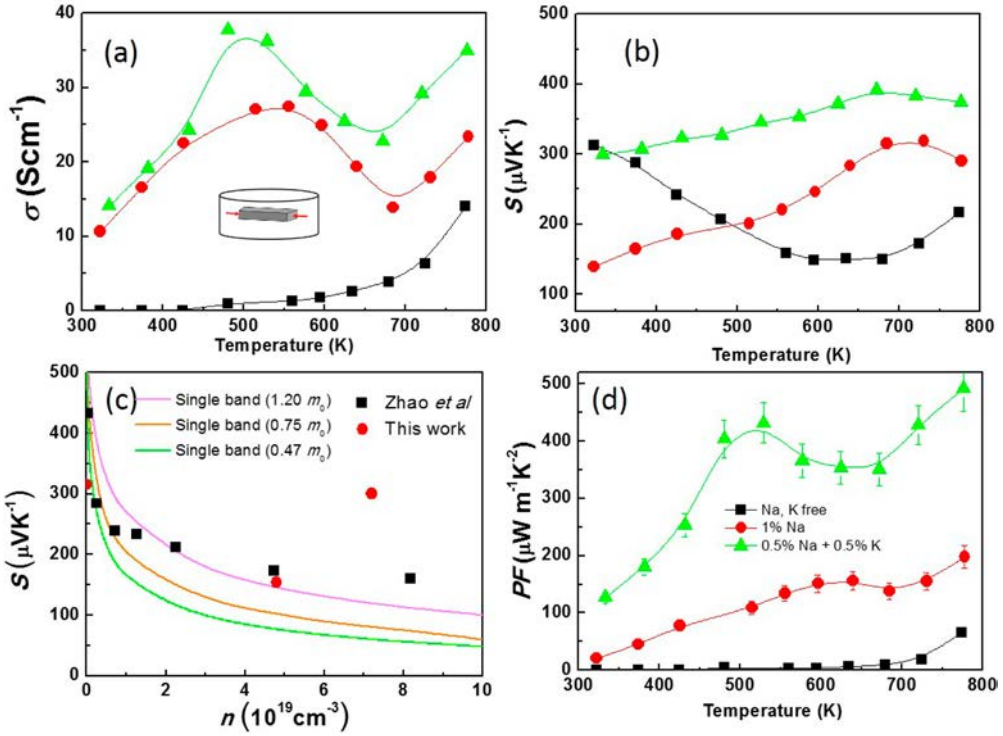

Figure 4. Electrical transport properties of undoped, 1% Na-doped, and (0.5% Na+0.5% K)-codoped SnSe: (a) electrical conductivity, (b) Seebeck coefficient, (c) Seebeck coefficient as a function of Hall carrier concentration at room temperature (red circles, experimental measurements from the present work; black squares, experimental measurements from Zhao et al.[23]), and (d) power factor.

shown in Figure S4. The carrier concentrations indicate that the Fermi level was shifted downward more in the (0.5% Na+0.5% K)-codoped sample than that in the Na-doped sample, or that the solid solubility of the dopants in SnSe was higher in the (0.5% Na+0.5% K)-codoped sample than in the Na-doped sample, in agreement with the DFT calculations of band structure and solid solubility. The temperature dependence of σ was also altered significantly by doping, with undoped SnSe exhibiting semiconducting thermally activated transport behavior. In the doped samples, σ exhibited a similar trend, first increasing until ~560 K (480 K for the (0.5% Na+0.5% K)-codoped sample, as the Fermi level was shifted more strongly into the valence bands in the (0.5% Na+0.5% K)-codoped sample, first turning it into a metal; see the band structure), indicating a semiconductor-like behavior, and then decreasing until about 680 K (for K-doped, 594 K), typically showing a metal-like behavior, and lower again at higher temperatures due to the thermal excitation of minority carriers. The Hall mobilities in all three samples were low compared to that in a single crystal and stayed at a low level of below 3.0 $cm^2 V^{-1}s^{-1}$ as a result of a grain-boundary potential effect[15] due to the presence of nanoprecipitates within the grains, as observed in conventional TEM images.

Figure 2b shows that the Seebeck coefficient in undoped SnSe has a temperature dependence similar to that reported previously,[15] decreasing to 634 K, reaching a minimum of 150 $\mu V\ K^{-1}$, and then increasing. In contrast, the Seebeck coefficient in the Na-doped and (Na,K)-codoped samples exhibited different behavior, increasing to maxima of 318 and 383 $\mu V\ K^{-1}$ at ~700 K for the Na-doped and (0.5% Na+0.5% K)-codoped samples, respectively. As a consequence of the simultaneously enhanced electrical conductivity and Seebeck coefficient, the power factor in the (0.5% Na+0.5% K)-codoped sample reached the highest value of 492 μ W m^{-1} K^{-2} at 773 K, whereas the corresponding power factors were 65 and 284 μW m^{-1} K^{-2} at 773 K for the undoped and 1% Na-doped samples, respectively. The highest power factor of 492 at 773 K is 8 times higher than that of the undoped sample. Figure 4c shows the Pisarenko line (Seebeck coefficient vs carrier concentration) calculated using a single parabolic band (SPB) model, as well as a comparison between the fitting results and the experimental measurements from this work and a previous work over a wide range of carrier concentrations. Our results match very well for undoped SnSe for a density-of-states (DOS) effective mass of 0.47 m_e. The Seebeck coefficient for 1% Na-doped SnSe deviates from the Pisarenko line for 0.47 m_e and falls onto the line for 1.20 m_e. The enhancements in Seebeck coefficient and DOS effective mass are consistent with the decreasing energy offsets for VB1 and VB2. Significantly, the Seebeck coefficient was enhanced twice for the (Na,K)-codoped sample as a result of the presence of complex multiple valleys in the valence band, as shown by the DFT calculations (Figure 3), with smaller energy gaps between the valence bands.

2.4. Reducing the Thermal Conductivity through the Introduction of Defects. The total thermal conductivity was lower after doping even though there was an additional contribution from carriers, suggesting that another phonon scattering mechanism was present, such as point defects. The total thermal conductivities at 323 K were 0.94, 0.81, and 0.55 W m^{-1} K^{-1} for the undoped, 1% Na-doped, and (0.5% Na +0.5% K)-codoped samples, respectively. The values decreased monotonically with increasing temperature, reaching minima of 0.48, 0.44, and 0.32 W m^{-1} K^{-1} for the undoped, 1% Na-doped, and (0.5% Na+0.5% K)-codoped samples, respectively, at 773 K. These values are comparable to those reported for single crystals[6,10] and polycrystals[15,26] in previous reports. The

DOI: 10.1021/jacs.7b05339
J. Am. Chem. Soc. 2017, 139, 9714−9720

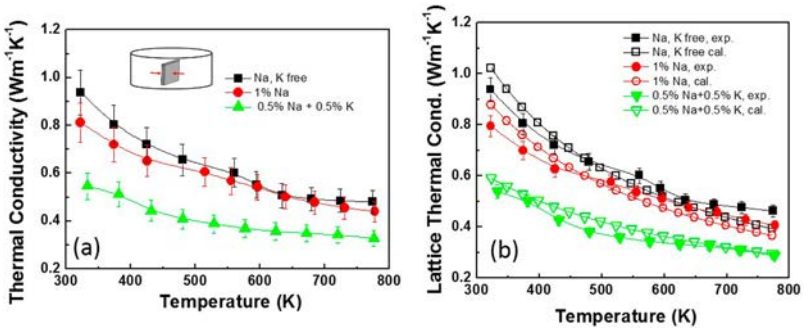

Figure 5. Temperature dependence of the thermal transport properties in all of the bulk samples. (a) Total thermal conductivity. (b) Lattice thermal conductivity. Experimental measurements are shown using solid symbols, whereas calculations are shown using open symbols.

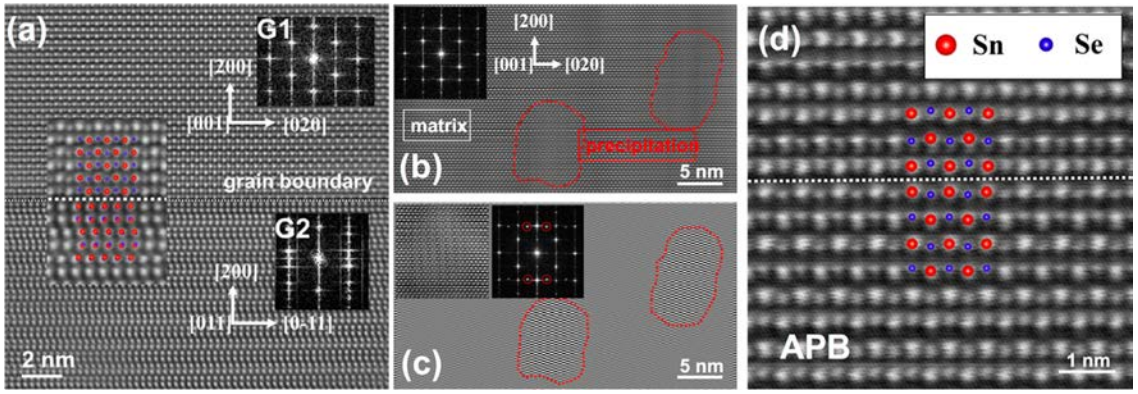

Figure 6. Atomic structure of defects in the (0.5% Na+0.5% K)-codoped sample. (a) Typical grain boundary between grain1 (G1) and grain 2 (G2) with orientations of [001] and [011], respectively. The insets show the FFTs of the two grains. The atomic structure and atomic model of the grain boundary are enlarged. The white dotted line indicates the position of grain boundary. (b) Precipitates embedded in the SnSe matrix. The insets show the FFTs of the matrix. The precipitates are marked with red dotted lines. (c) iFFT of panel b to separate the precipitates from the matrix by selecting the extra diffraction spot marked with red circles in the inset. The atomic structure of one precipitate is enlarged. (d) Antiphase boundary (APB) and corresponding atomic model in the {100} planes with $^1/_2$[010] crystal translation.

electrical thermal conductivity κ_e can be estimated according to the Wiedemann–Franz law $\kappa_e = LT\sigma$, where L is the Lorenz number. The calculation of L was estimated in a single parabolic band model (resulting in a value of L with a deviation of less than 10% when compared with a more rigorous single nonparabolic band and multiple band model calculations), as described elsewhere.[23] The calculation results and details of L are shown in Figure S3. After subtraction of the contribution from carriers, the lattice thermal conductivity showed a similar $1/T$ temperature dependence, which can be attributed to Umklapp scattering. The lattice thermal conductivity was almost the same as the thermal conductivity for all of the samples at 323 K, whereas at 773 K, the values were 0.46, 0.41, and 0.29 W m^{-1} K^{-1} for the undoped, 1% Na-doped, and (0.5% Na+0.5% K)-codoped samples, respectively. The lattice thermal conductivity was lowest in the (0.5% Na+0.5% K)-codoped sample, followed by the Na-doped and undoped samples, suggesting that K doping is more effective at scattering phonons based on Na doping.

In combination with the TEM structural parameters and the estimated point defect contents in the three samples, we performed calculations of lattice thermal conductivity using Callaway's model[29] (see details in the Supporting Information), including contributions from Umklapp scattering, the normal phonon–phonon process, and point defects. Given that the TEM analysis was performed on localized areas in the samples, we assigned a solubility range instead of an exact number to the point-defect contribution. The lattice thermal conductivity in the 1% Na-doped sample was almost fitted by a 0.25% Na solid solubility (estimated from the carrier concentration), keeping the other parameters the same. It should be noted that the precipitates in all of the samples contributed little to the scattering of phonons, as a result of the short mean free path of phonons of several nanometers in SnSe with a high Grüneisen parameter;[6−8] that is, atomic-scale point defects dominate phonon scattering. Therefore, for the sake of increasing the solid solubility of Na and K in the (0.5% Na+0.5% K)-codoped sample, more K and Na (as estimated from the carrier concentration, ∼0.4%) substituted for Sn in the matrix and scattered phonons more strongly, leading to a lower lattice thermal conductivity, as shown in the green profiles in Figure 5b. However, the experimental results are 15% lower than the calculated values based on the above scattering mechanisms in the (0.5% Na+0.5% K)-codoped sample, suggesting that additional scattering mechanisms contribute to phonon transport.

In addition to the low-magnification TEM images shown in Figure 2, atomically resolved aberration-corrected STEM images were used to identify the atomic structures of defects in the (0.5% Na+0.5% K)-codoped sample, which could serve as effective scattering centers for phonons with different wavelengths. Figure 6a shows a grain boundary marked by a white dotted line. In addition to a grain boundary associated with a large misorientation or dislocations, as reported for almost all polycrystalline thermoelectric materials, a boundary is also observed here. The orientation relationship was

DOI: 10.1021/jacs.7b05339
J. Am. Chem. Soc. 2017, 139, 9714–9720

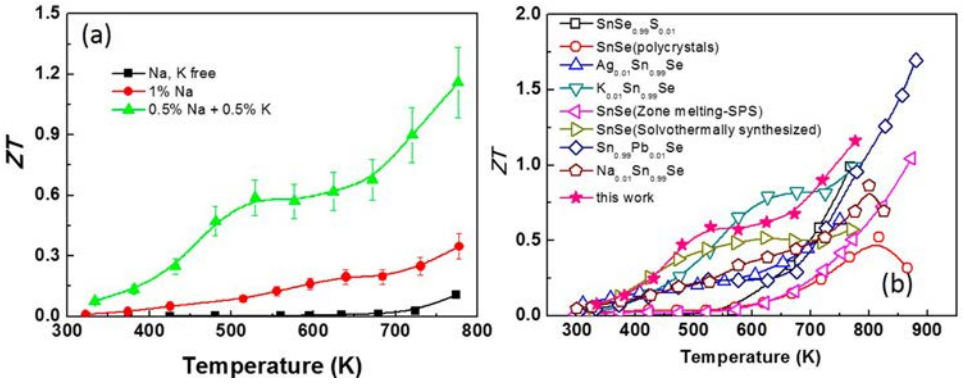

Figure 7. Temperature dependence of *ZT* for (a) all of the bulk samples and (b) reported SnSe polycrystalline materials [$SnSe_{0.99}S_{0.01}$,[18] SnSe (polycrystal),[27] $Ag_{0.01}Sn_{0.99}Se$,[17] $K_{0.01}Sn_{0.99}Se$,[15] SnSe (zone melting SPS),[28] SnSe (solvothermally synthesized),[29] $Sn_{0.99}Pb_{0.01}Se$,[24] $Na_{0.01}Sn_{0.99}Se$[16]].

determined to be $[001]_{G1}//[011]_{G2}$, $[200]_{G1}//[200]_{G2}$, $[020]_{G1}//[0\bar{1}1]_{G2}$ through an analysis of the fast Fourier transform (FFT) shown as an inset in Figure 6a. An atomic model of the grain boundary is enlarged in the inset. The misfit along the $[020]_{G1}$ or $[0\bar{1}1]_{G2}$ directions is estimated to be ~2.6%. No dislocations were found, indicating an unrelaxed strain field across the boundary. Nanoscale precipitates were distributed widely in the (0.5% Na+0.5% K)-codoped sample. We used an inverse FFT (iFFT) to separate the precipitates from the matrix, as shown in Figure 6b,c, by selecting the extra diffraction spots that are marked by red circles in the inset in Figure 6c. The precipitate was coherent with the matrix. The enlarged atomic structure in the precipitate is shown in the inset to Figure 6c, although the blurred atomic planes make it difficult to determine the crystal structure directly from the image. Antiphase boundary (APB) defects were observed in the (0.5% Na+0.5% K)-codoped sample. The APB was observed on {100} planes, involving a $^1/_2[010]$ crystal translation, as shown in Figure 6d. Such planar defects are easily formed in layered structures and can act as scattering centers to lower the thermal conductivity. It is reasonable that these additional structural defects, alongside point defects, might contribute to the effective scattering of phonons, further alleviating the lattice thermal conductivity in the (0.5% Na+0.5% K)-codoped SnSe sample.

By increasing the power factor through a multivalley effect by band engineering and by the enhancement of phonon scattering by defects in (0.5% Na+0.5% K)-codoped polycrystalline SnSe, we were able to increase the thermoelectric figure of merit *ZT* from ~0.1 and 0.3 in undoped and 1% Na-doped SnSe, respectively, to ~1.2 in (0.5% Na+0.5% K)-codoped SnSe at 773 K. The *ZT* value of the codoped sample is 1 order of magnitude higher than that of the undoped sample at 773 K, as shown in Figure 7a. Figure 7b shows the temperature dependence of *ZT* in the present work and for other SnSe polycrystalline samples. The *ZT* value of our (Na,K)-codoped sample reached the highest value of 1.2 at 773 K when compared to all of the other samples.[15−18,27−29] Based on measurements of the areas under the curves, (0.5% Na+0.5% K)-codoped SnSe also had the highest average *ZT* value between 373 and 773 K. Pb-doped polycrystalline SnSe has the highest *ZT* value of 1.6 at 900 K.[24] However, in our work, the SnSe sample became soft above 773 K, perhaps because mechanical alloying produces nanograin sizes with large active surfaces.

3. CONCLUDING REMARKS

(Na,K)-codoped polycrystalline SnSe was prepared by mechanical alloying and spark plasma sintering. The dimensionless figure of merit *ZT* increased from 0.1 and 0.3 for undoped and 1% Na-doped polycrystalline SnSe to 1.2 for 1% (Na,K)-codoped polycrystalline SnSe. This increase resulted from a significant enhancement in Seebeck coefficient due to multivalley effects and a decrease in lattice thermal conductivity due to the enhanced solid solubility of Na and K in the (0.5% Na+0.5% K)-codoped sample, as well as the presence of additional atomic-scale structure defects. Our results provide a new synergistic doping strategy for enhancing the thermoelectric performance of polycrystalline SnSe. The present method is also suitable for enhancing performance for any other thermoelectric systems.

■ ASSOCIATED CONTENT

Supporting Information

The Supporting Information is available free of charge on the ACS Publications website at DOI: 10.1021/jacs.7b05339.

XRD patterns (in-plane and out-of-plane) and lattice parameters of undoped, 1% Na-doped, and 0.5% Na + 0.5% K codoped samples (Figure S1); FESEM images of undoped, 1% Na-doped, and 0.5% Na + 0.5% K codoped samples (Figure S2); temperature dependences of electrical conductivity, Seebeck coefficient, thermal conductivity, and *ZT* value for 0.5% Na + 0.5% K codoped sample in the directions perpendicular and parallel to the pressing direction (Figure S3); temperature dependences of thermal diffusivity, Lorenz number, carrier thermal conductivity, and lattice thermal conductivity for undoped, 1% Na-doped, and 0.5% Na + 0.5% K codoped SnSe (Figure S4); carrier concentrations and carrier mobilities of the three bulk samples (Figure S5). Measured and relative densities of all of the bulk samples (Table S1); SnSe and ASe (A = Na, K) formation energies; chemical potential differences between A and Sn; "raw" Na, K, and Na + K defect formation energies; and Na, K, and Na + K defect formation energies calculated for the systems SnSe−ASe with A = Na, K (Table S2); parameters for lattice thermal conductivity calculations (Table S3); atomic information for point defects (Table S4); details of the experimental section including sample synthesis and property measurements (PDF)

DOI: 10.1021/jacs.7b05339
J. Am. Chem. Soc. 2017, 139, 9714−9720

AUTHOR INFORMATION

Corresponding Authors

*f.zheng@fz-juelich.de.
*jingfeng@kmust.edu.cn.
*zhaolidong@buaa.edu.cn.

ORCID

Zhen-Hua Ge: 0000-0001-8810-5103
Fengshan Zheng: 0000-0001-7354-041X
Lei Jin: 0000-0001-6924-2364
Li-Dong Zhao: 0000-0003-1247-4345

Author Contributions

‡Z.-H.G., D.S., and X.C. contributed equally to this work.

Notes

The authors declare no competing financial interest.

ACKNOWLEDGMENTS

This work was supported by the National Natural Science Foundation of China (Grants 51501086 and 51571007), the Beijing Municipal Science & Technology Commission (Grant Z171100002017002), and the Shenzhen peacock plan team (Grant KQTD2016022619565911).

REFERENCES

(1) Tan, G. J.; Zhao, L. D.; Kanatzidis, M. G. *Chem. Rev.* **2016**, *116*, 12123.
(2) Pei, Y.; Shi, X.; LaLonde, A.; Wang, H.; Chen, L.; Snyder, G. J. *Nature* **2011**, *473*, 66.
(3) Heremans, J. P.; Jovovic, V.; Toberer, E. S.; Saramat, A.; Kurosaki, K.; Charoenphakdee, A.; Yamanaka, S.; Snyder, G. J. *Science* **2008**, *321*, 554.
(4) Biswas, K.; He, J. Q.; Blum, I. D.; Wu, C. I.; Hogan, T. P.; Seidman, D. N.; Dravid, V. P.; Kanatzidis, M. G. *Nature* **2012**, *489*, 414.
(5) Toberer, E. S.; Zevalkink, A.; Snyder, G. J. *J. Mater. Chem.* **2011**, *21*, 15843.
(6) Zhao, L.-D.; Lo, S. H.; Zhang, Y. S.; Sun, H.; Tan, G. J.; Uher, C.; Wolverton, C.; Dravid, V. P.; Kanatzidis, M. G. *Nature* **2014**, *508*, 373.
(7) Li, C. W.; Hong, J.; May, A. F.; Bansal, D.; Chi, S.; Hong, T.; Ehlers, G.; Delaire, O. *Nat. Phys.* **2015**, *11*, 1063.
(8) Xiao, Y.; Chang, C.; Pei, Y.; Wu, D.; Peng, K.; Zhou, X.; Gong, S.; He, J.; Zhang, Y.; Zeng, Z.; Zhao, L.-D. *Phys. Rev. B: Condens. Matter Mater. Phys.* **2016**, *94*, 125203.
(9) Loa, I.; Husband, R. J.; Downie, R. A.; Popuri, S. R.; Bos, J. W. *J. Phys.: Condens. Matter* **2015**, *27*, 072202.
(10) Zhao, L.-D.; Tan, G.; Hao, S.; He, J. Q.; Pei, Y.; Chi, H.; Wang, H.; Gong, S.; Xu, H.; Dravid, V.; Uher, C.; Snyder, J.; Wolverton, C.; Kanatzidis, M. G. *Science* **2016**, *351*, 141.
(11) Peng, K.; Lu, X.; Zhan, H.; Hui, S.; Tang, X.; Wang, G.; Dai, J.; Uher, C.; Wang, G.; Zhou, X. *Energy Environ. Sci.* **2016**, *9*, 454.
(12) Wei, T. R.; Wu, C. F.; Zhang, X.; Tan, Q.; Sun, L.; Pan, Y.; Li, J. F. *Phys. Chem. Chem. Phys.* **2015**, *17*, 30102.
(13) Chere, E. K.; Zhang, Q.; Dahal, K.; Cao, F.; Mao, J.; Ren, Z. *J. Mater. Chem. A* **2016**, *4*, 1848.
(14) Leng, H.-Q.; Zhou, M.; Zhao, J.; Han, Y.-M.; Li, L.-F. *RSC Adv.* **2016**, *6*, 9112.
(15) Chen, Y.-X.; Ge, Z.-H.; Yin, M.; Feng, D.; Huang, X.-Q.; Zhao, W.; He, J. *Adv. Funct. Mater.* **2016**, *26* (37), 6836.
(16) Wei, T.-R.; Tan, G.; Zhang, X.; Wu, C.-F.; Li, J.-F.; Dravid, V. P.; Snyder, G. J.; Kanatzidis, M. G. *J. Am. Chem. Soc.* **2016**, *138* (28), 8875.
(17) Chen, C.-L.; Wang, H.; Chen, Y.-Y.; Day, T.; Snyder, G. J. *J. Mater. Chem. A* **2014**, *2*, 11171.
(18) Zhang, Q.; Chere, E. K.; Sun, J.; Cao, F.; Dahal, K.; Chen, S.; Chen, G.; Ren, Z. *Adv. Energy Mater.* **2015**, *5* (12), 1500360.
(19) Chang, C.; Tan, Q.; Pei, Y.; Xiao, Y.; Zhang, X.; Chen, Y.-X.; Zheng, L.; Gong, S.; Li, J.-F.; He, J.; Zhao, L.-D. *RSC Adv.* **2016**, *6* (100), 98216.
(20) Wang, X.; Xu, J.; Liu, G.; Fu, Y.; Liu, Z.; Tan, X.; Shao, H.; Jiang, H.; Tan, T.; Jiang, J. *Appl. Phys. Lett.* **2016**, *108*, 083902.
(21) Kresse, G.; Furthmüller, J. *Phys. Rev. B: Condens. Matter Mater. Phys.* **1996**, *54*, 11169.
(22) Pei, Y.; Wang, H.; Snyder, G. J. *Adv. Mater.* **2012**, *24*, 6125.
(23) Zhao, L.-D.; Chang, C.; Tan, G.; Kanatzidis, M. G. *Energy Environ. Sci.* **2016**, *9*, 3044.
(24) Tang, G.; Wei, W.; Zhang, J.; Li, Y.; Wang, X.; Xu, G.; Chang, C.; Wang, Z.; Du, Y.; Zhao, L.-D. *J. Am. Chem. Soc.* **2016**, *138*, 13647.
(25) He, J.; Zhao, L.-D.; Zheng, J.-C.; Doak, J. W.; Wu, H.; Wang, H.-Q.; Lee, Y.; Wolverton, C.; Kanatzidis, M. G.; Dravid, V. P. *J. Am. Chem. Soc.* **2013**, *135*, 4624.
(26) Callaway, J. *Phys. Rev.* **1959**, *113*, 1046.
(27) Sassi, S.; Candolfi, C.; Vaney, J. B.; Ohorodniichuk, V.; Masschelein, P.; Dauscher, A.; Lenoir, B. *Appl. Phys. Lett.* **2014**, *104*, 212105.
(28) Fu, Y.; Xu, J.; Liu, G. Q.; Yang, J.; Tan, X.; Liu, Z.; Qin, H.; Shao, H.; Jiang, H.; Liang, B.; Jiang, J. *J. Mater. Chem. C* **2016**, *4*, 1201.
(29) Li, Y.; Li, F.; Dong, J.; Ge, Z. H.; Kang, F. Y.; He, J. Q.; Du, H.; Li, B.; Li, J. F. *J. Mater. Chem. C* **2016**, *4*, 2047.
(30) Barthel, J. *Dr. Probe - High-Resolution (S)TEM Image Simulation Software*; Ernst Ruska-Centre (ER-C) for Microscopy and Spectroscopy with Electrons: Jülich, Germany, 2017; http://www.er-c.org/barthel/drprobe/ (accessed Jan 20, 2017).
(31) Kovács, A.; Schierholz, R.; Tillmann, K. *JLSRF* **2016**, *2*, A43.

DOI: 10.1021/jacs.7b05339
J. Am. Chem. Soc. 2017, 139, 9714−9720